Acta Materialia 279 (2024) 120300

Contents lists available at ScienceDirect

Acta Materialia

journal homepage: www.elsevier.com/locate/actamat

Hierarchical nanolayered structures-enabled record-high fracture resistant zircaloy

Xiao-Wei Zou [a], Irene J. Beyerlein [b,c,1], Wei-Zhong Han [a,*]

[a] Center for Advancing Materials Performance from the Nanoscale, State Key Laboratory for Mechanical Behaviour of Materials, Xi'an Jiaotong University, Xi'an 710049, PR China
[b] Department of Mechanical Engineering, University of California, Santa Barbara, CA 93106-5070, USA
[c] Materials Department, University of California, Santa Barbara, CA 93106-5070, USA

ARTICLE INFO

Keywords:
Zircaloy
Fracture resistance
Hierarchical
Interface
Dislocation

ABSTRACT

As a widely used nuclear structural material, zirconium (Zr) alloys are susceptible to brittle hydride-induced cracking. The intrinsic inability to arrest this cracking tendency in Zr poses a significant threat to the service safety of Zr cladding tubes. Here, we propose a microstructural design strategy, by introducing a hierarchical nanolayered duplex-phase structure in the Zr-2.5Nb alloy, to effectively inhibit the propagation of cracks. An unprecedented fracture toughness of $K_{JIc} \sim 165$ MPa·m$^{1/2}$, corresponding to $J_{Ic} \sim 256$ kJ/m^2, is achieved due to the uniform and dense plastic deformation that develops ahead of the crack tip, which is uncharacteristic of Zr-based materials. Our analysis reveals that the effective crack tip blunting occurs because the high density of multiply oriented α/β interfaces in the hierarchical Zr-2.5Nb alloy stimulates ample <c+a> dislocations and facilitates deformation twin nucleation, both of which are challenging to activate in conventional Zr-based materials at room temperature. The exceptional fracture toughness enabled by the hierarchical nanolayered structure provides a new pathway to designing damage-tolerant hexagonal metals for safety-critical applications.

1. Introduction

Zirconium (Zr) alloys are widely used in the nuclear industry as fuel cladding tubes and structural components due to their low thermal neutron capture cross-section, excellent corrosion resistance and superior mechanical properties [1-3]. However, while in service in nuclear reactors, Zr alloys commonly produce hydrides [4,5], which are brittle phases with extremely low fracture toughness (<1 MPa·m$^{1/2}$) [6]. The precipitation of these hydrides makes the Zr cladding susceptible to microcracking [7], that can limit lifetime in service and present a safety hazard. One solution receiving intense consideration focuses on enhancing the fracture toughness of the Zr alloy itself, so that rapid propagation of hydride-induced cracks can be inhibited [5].

The mechanisms usually associated with enhancing fracture toughness in alloys are classified as either intrinsic or extrinsic [8]. Intrinsic toughening involves suppressing formation of damage in the form of microcracks or voids ahead of a crack tip by enhancing plastic deformation capacity [8]. Extrinsic toughening acts instead in the wake of the crack through mechanisms, like crack bridging, that resist the crack from opening and the local stresses ahead of the crack tip from rising [9]. For metallic materials, intrinsic toughening plays a more critical role as it can simultaneously hinder both crack initiation and propagation [8]. Improving the fracture resistance of Zr alloys thus calls for enhancing the plastic deformation capacity ahead of the crack tip so that damage is thwarted.

As a hexagonal close-packed (HCP) metal, the plastic deformation of Zr is primarily provided by dislocation slip and twinning [10]. The crystallography of the dominant slip mode is $\{10\bar{1}0\}\langle 1\bar{2}10\rangle$ slip, known as prismatic <a> slip, due to its lowest critical resolved shear stress (CRSS) of ~20 MPa at room temperature [11]. However, the prismatic <a> slip mode can only accommodate plasticity along the <a>-axis and it consists of only two independent slip systems [12]. Thus, a Zr crystal embedded within a polycrystal cannot deform by prismatic <a> slip alone and satisfy the Taylor-von Mises criterion for uniform plastic deformation, which requires at least five independent slip systems [13,14]. Twinning in HCP crystals acts in addition to slip

* Corresponding author.
E-mail address: wzhanxjtu@mail.xjtu.edu.cn (W.-Z. Han).
[1] Irene J. Beyerlein was an Editor of the journal during the review period of the article. To avoid a conflict of interest, Irene J. Beyerlein was blinded to the record and another editor processed this manuscript.

https://doi.org/10.1016/j.actamat.2024.120300
Received 20 May 2024; Received in revised form 14 August 2024; Accepted 15 August 2024
Available online 23 August 2024
1359-6454/© 2024 Acta Materialia Inc. Published by Elsevier Ltd. All rights are reserved, including those for text and data mining, AI training, and similar technologies.

and is a <c>-axis deformation mechanism; however, unlike slip, all twin modes are unidirectional, and any given mode can either accommodate <c>-contraction or extension but not both. Therefore, compared to twinning, the activation of <c+a> dislocation slip, which commonly occurs on the first-order pyramidal $\{1\bar{1}01\}$ planes with a Burgers vector $\vec{b}=1/3<\bar{1}\bar{1}23>$ [15,16], is the more favorable <c>-axis deformation mechanism. The first-order pyramidal <c+a> slip mode, which contains 12 slip systems, can contribute the slip systems needed to accommodate uniform deformation [16,17]. Unfortunately, the CRSS of <c+a> slip is typically 10 times higher than that of <a> slip in Zr [11,15], resulting in much lower activity of <c+a> dislocations.

In addition, recent in-situ TEM analysis [16] and atomic simulations [18] have reported that the mobility of the edge component of <c+a> dislocations in HCP metals is much lower than that of the screw component. This noticeable difference in mobility can hinder the multiplication of <c+a> dislocations in Zr alloys [19], further reducing their activity. It has been confirmed that the addition of alloying elements can promote <c>-axis deformation by facilitating <c+a> dislocation cross-slip [20]. However, this mechanism may contribute minimally to the multiplication of <c+a> dislocations. Therefore, creating sufficient homogeneous deformation ahead of the crack tip in Zr alloys by enhancing the activity of <c+a> dislocations remains the key challenge.

In this work, we propose a strategy to enhance the activity of <c+a> dislocations at the crack tip in Zr alloys by directly introducing <c+a> dislocations sources. A unique hierarchical nanolayered duplex-phase structure with high density of α/β-Zr interfaces has been incorporated into Zr-2.5Nb alloy. We show that these interfaces serve as sources for <c+a> dislocations, facilitating the nucleation of numerous <c+a> dislocations and significantly enhancing plastic deformation capacity ahead of the crack tip. The α/β-Zr interfaces also assist in activating multiple deformation twins that can provide extra <c>-axis deformation to help effectively blunt the crack tip. Consequently, compared to coarse-grained pure Zr and coarse-layered Zr-2.5Nb, the hierarchical nanolayered Zr-2.5Nb alloy achieves exceptional fracture resistance at ambient temperature.

2. Materials and methods

2.1. Sample preparation

The hierarchical nanolayered Zr-2.5Nb alloy (NL Zr-2.5Nb) was fabricated using the dynamic thermal-mechanical phase transformation (DTMPT) method [21]. Initial cylindrical samples 18 mm in diameter and 27 mm in height were cut from the as-cast Zr-2.5 wt. % Nb ingot. Subsequently, hot uniaxial compression with a strain rate of 1/s and a total thickness reduction of 70 % was conducted using DSI Gleeble 3800 thermomechanical simulator at 950°C before air cooling. One piece of as-cast Zr-2.5Nb alloy was annealed at 1000°C for 30 min, followed by air cooling to room temperature to obtain the coarse-layered (CL) Zr-2.5Nb alloy. To obtain the pure Zr sample for comparison, a pure Zr sheet was annealed at 820°C for 72 h using a tube furnace with a vacuum of 1.3×10^{-4} Pa.

2.2. Mechanical properties test

Rectangular dog-bone shaped tensile samples with a gauge length of 14 mm and a gauge cross-section of 1.5 mm × 3.4 mm were cut by electrical discharge machining (EDM) (Fig. S1). Quasi-static uniaxial tensile tests were performed on a SANS CMT4104 testing machine with a strain rate of 1.0×10^{-3}/s. The tensile axis lies parallel to the radial direction (RD) of the cylindrical NL Zr-2.5Nb sample (Fig. S1(a)). All tensile tests were conducted using a 10-mm extensometer to measure the strain.

To evaluate the fracture toughness, single edge bend (SEB) specimens with a thickness (B) of 5 mm, a width (W) of 8 mm, and total length (L) of 36 mm, were fabricated from the NL Zr-2.5Nb, CL Zr-2.5Nb and pure Zr samples (Fig. S1(a)). For the NL Zr-2.5Nb alloy, SEB specimens were cut along the RD of cylindrical sample (Fig. S1(a)). Notches with a depth of 2.8 mm and a root radius of ~100 μm, were cut in all SEB specimens. All SEB samples were fatigue pre-cracked to obtain a total crack length of a_0 = 3.6 mm (~ 0.45 W). Fracture toughness test was conducted using elastic-plastic fracture mechanics method in accordance with ASTM Standard E1820 [22]. The crack-resistance curves (J-R curves), i.e., J as a function of the stable crack extension Δa were measured at room temperature (see details in Supplementary Materials).

2.3. Microstructural characterization

Microstructural characteristics of various as-processed Zr samples, and the crack-path morphologies along the crack propagation direction on specimen surface and mid-plane were examined using a Hitachi SU-6600 scanning electron microscope (SEM) operating in secondary electron (SE) imaging mode. To characterize the fracture and deformation morphologies on the sample surface and mid-plane, the three types of Zr samples were ground and mechanically polished. The mid-plane of CL Zr-2.5Nb and NL Zr-2.5Nb specimens were further etched using a mixture of 10 vol. % hydrofluoric acid, 40 vol. % nitric acid, and 50 vol. % distilled water for microstructural and crack-path characterizations. Electron back-scatter diffraction (EBSD) scans were further performed near the crack path on the mid-plane using the Oxford Instrument HKL equipped with Channel-5 software, operated at an accelerating voltage of 20 kV with a step size of 0.5 – 4 μm. Samples for EBSD were electrochemically polished using a 10 vol. % perchloric acid, 70 vol. % methyl alcohol, and 20 % ethylene glycol monobutyl ether solution with a voltage of 20 V at -30°C.

To reveal the dislocation structures within the plastic zone ahead of the crack tip under plane-strain conditions in the three types of Zr samples, SEB specimens with a crack extension of Δa ~ 1 mm were used to cut thin foils at the mid-plane using EDM and then mechanically ground down to about 50 μm. Discs with 3 mm in diameter containing the crack tip were punched and dimpled in the centre, followed by twin-jet electrochemical polishing under an operation voltage of 25 V at -40°. The polishing electrolyte is a mixture of 10 vol. % perchloric acid and 90 vol. % ethanol. The observation region was carefully selected to ensure that it is located within the plastic zone ahead of the crack tip. The characterizations of dislocation structures were carried out using a FEG JEOL 2100F high resolution-transmission electron microscope (TEM) at 200 kV with a double tilt holder. High angle annular dark-field scanning transmission electron microscopy (HAADF-STEM) was further performed using a spherical-aberration-corrected STEM (Hitachi HF5000) with an accelerating voltage of 200 kV to uncover the α/β interface structure of NL Zr-2.5Nb.

3. Results

3.1. Initial microstructures

Fig. 1 presents the microstructures of the pure Zr, coarse-layered (CL) Zr-2.5Nb, and hierarchical nanolayered (NL) Zr-2.5Nb samples. Pure Zr consists of equiaxed grains with an average grain size of ~70 μm, as shown in Fig. 1 (a). The average grain size of the CL Zr-2.5Nb alloy is significantly larger than 100 μm. The CL Zr-2.5Nb alloy displays a coarse colony structure featuring relatively high aspect ratio colonies within the grains ranging approximately from 20 to 100 μm in size. An example of the rough boundaries of one α/β duplex-phase colony is outlined by white dashed lines in Fig. 1 (b). The colonies consist of alternating hexagonal-close-packed (HCP) α-Zr lamellae (average thickness of ~511 nm) and body-centred-cubic (BCC) β-Zr lamellae (average thickness of ~66 nm).

By contrast, the NL Zr-2.5Nb alloy exhibits a network of nanolayers

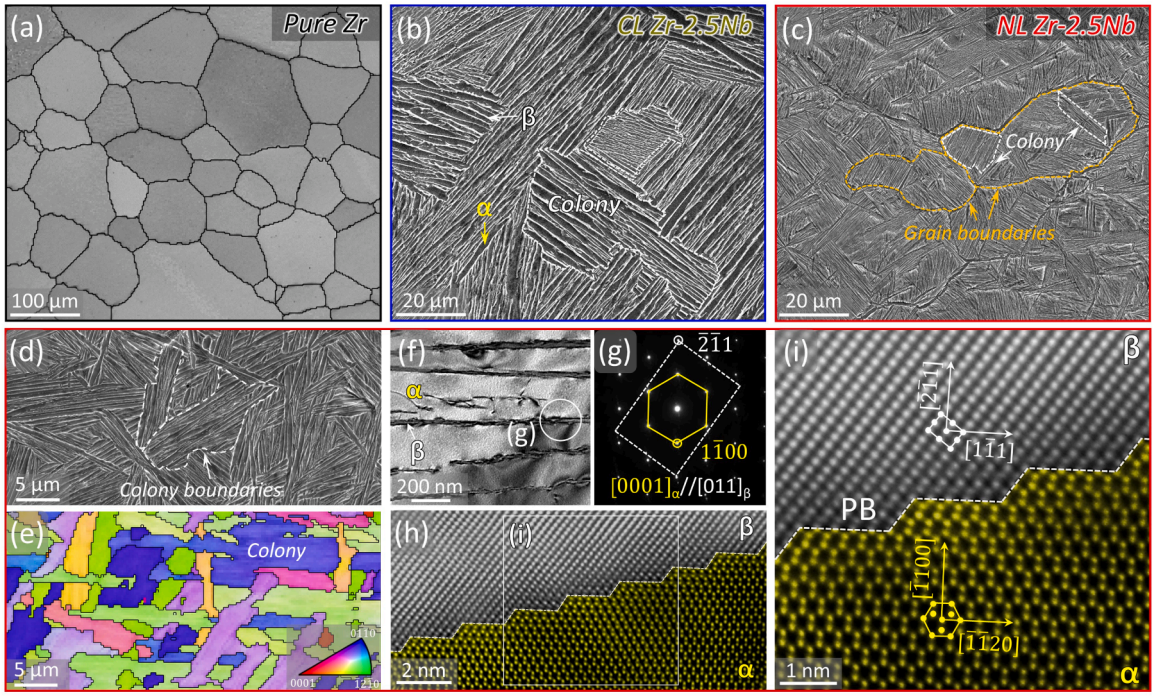

Fig. 1. Microstructure characterization of pure Zr, coarse-layered (CL) Zr-2.5Nb, and nano-layered (NL) Zr-2.5Nb. (a) EBSD band contrast (BC) map showing the equiaxed-grain structure of pure Zr. (b) SEM image showing the coarse-layered α/β-Zr duplex-phase structure of CL Zr-2.5Nb. The colony boundaries are outlines by white dashed lines. (c, d) SEM images showing the hierarchical nanolayered duplex-phase structure of NL Zr-2.5Nb. Example grain boundaries (GBs) are outlined by orange dashed lines and the micro-colony boundaries in one example grain are outlined in white. (e) EBSD inverse pole figure (IPF) image of the NL Zr-2.5Nb showing a consistent orientation of α-Zr layers within the micro-colonies. (f) A TEM image and (g) selected area diffraction patterns (SADPs) showing the Burgers orientation relationship between the α-Zr and β-Zr phases. (h) Low and (i) high magnificationHAADF-STEM along $[0001]_\alpha//[011]_\beta$ show the typical "terrace-ledge" α/β-Zr phase boundary (PB) structure, as marked by white dashed lines.

with a much higher density of α/β duplex-phase interfaces (Fig. 1 (c-f)). This alloy consists of coarse grains with a size of 20-100 μm, as outlined by orange dashed lines in Fig. 1 (c), and each grain is filled with not one, but several microscale colonies (Fig. 1 (c, d)). Based on the EBSD inverse pole figure (IPF) image (Fig. 1 (e)), all α-Zr lamellae within a single micro-colony display the same orientation, whereas orientations vary among neighbouring micro-colonies. Fig. 1 (f) shows a TEM image of the α/β-Zr phase nanostructure within a single micro-colony. It reveals that the fine size of the α-Zr layer (average thickness of ~188 nm) and nanoscale β-Zr layer (average thickness of ~22 nm). It is also observed from the selected area diffraction patterns (SADPs) in Fig. 1 (g) that the α/β-Zr interface exhibits a classical Burgers orientation relationship: $[0001]_\alpha//[011]_\beta$ and $(\bar{1}100)_\alpha//(\bar{2}\bar{1}1)_\beta$. When further using HAADF-STEM along the $[0001]_\alpha//[011]_\beta$ to characterize the phase boundary (PB), a typical "terrace-ledge" structure is observed (Fig. 1 (h, i)). For Zr-2.5Nb alloy at room temperature, the Nb content in the α-Zr and β-Zr phase is ~0.5 wt. % and ~20 wt. %, respectively [23]. The volume fraction of β-Zr phase has been calculated to be ~10 % [23]. In both our CL Zr-2.5Nb and NL Zr-2.5Nb sample, the Nb content, which stabilizes β-Zr phase, remains consistent. Both samples undergo phase transformation from the β-Zr single-phase region with air cooling and experience nearly identical cooling rate. Therefore, the volume fraction of the β-Zr lamella in both samples should be the same and ≈10 %. The reduced lamella thickness significantly increases the density of the β-Zr lamella in NL Zr-2.5Nb sample compared to CL Zr-2.5Nb sample, as shown in Fig. 1 (b, c).

3.2. Tensile and fracture properties

Fig. 2 compares the tensile properties and the fracture toughness among the three types of Zr samples. We measured engineering stress-strain curves at room temperature (Fig. 2 (a)). The yield strength significantly increases from 171 MPa in the pure Zr to 431 MPa in the CL Zr-2.5Nb and to 542 MPa in the NL Zr-2.5Nb, as shown in Table 1. Similarly, the ultimate tensile strength of the NL Zr-2.5Nb is the highest, at 648 MPa, which is 138 % higher than that of the pure Zr (272 MPa) and 20 % higher than that of the CL Zr-2.5Nb (538 MPa). For many traditional metallic materials, strengthening often leads to reductions in ductility—a well-known strength-ductility trade-off. Yet, remarkably, even with these increases in strength, the NL Zr-2.5Nb still maintains an excellent elongation to fracture of ~16 %. The nanolayered structure in the NL Zr-2.5Nb alloy clearly provides a desirable strength-ductility balance, which is not accessible with homogeneous pure Zr or CL Zr-2.5Nb with coarse-layered structures. The low strength and ductility of pure Zr were also reported in our previous study [24].

Nonlinear-elastic fracture mechanics analysis, based on *J*-integral as described in ASTM Standard E1820 [22], is adopted to assess the fracture toughness of the pure Zr, CL Zr-2.5Nb, and NL Zr-2.5Nb samples. Following the elastic compliance method, the force versus crack-mouth-opening displacement curves (Fig. S1(b)) obtained from SEB specimens are utilized to determine *J*-based R-curves, which give the *J*-integral as a function of crack extension Δa. According to the *J*-R curves shown in Fig. 2 (b), when compared to pure Zr and CL Zr-2.5Nb, the NL Zr-2.5Nb alloy displays the most pronounced toughening effect, characterized by much higher *J*-integral values and the clear rise in the *J*-R curve. NL Zr-2.5Nb achieves a superior *J*-based crack-initiation toughness of J_Q = 255.6 kJ·m^{-2} (Table 1), which is nearly 300 % and 56 % higher than that calculated in pure Zr (60.5 kJ·m^{-2}) and CL Zr-2.5Nb (163.7 kJ·m^{-2}), respectively.

According to the ASTM Standard E1820 [22], for the provisional toughness J_Q to be considered as a size-independent fracture toughness (J_{Ic}), specific validity criteria must be met for both *J*-field dominance and plane-strain conditions. These criteria require that $b_0, B > 10J_Q/\sigma_0$, where b_0, B, and σ_0 represent the initial ligament length, the sample

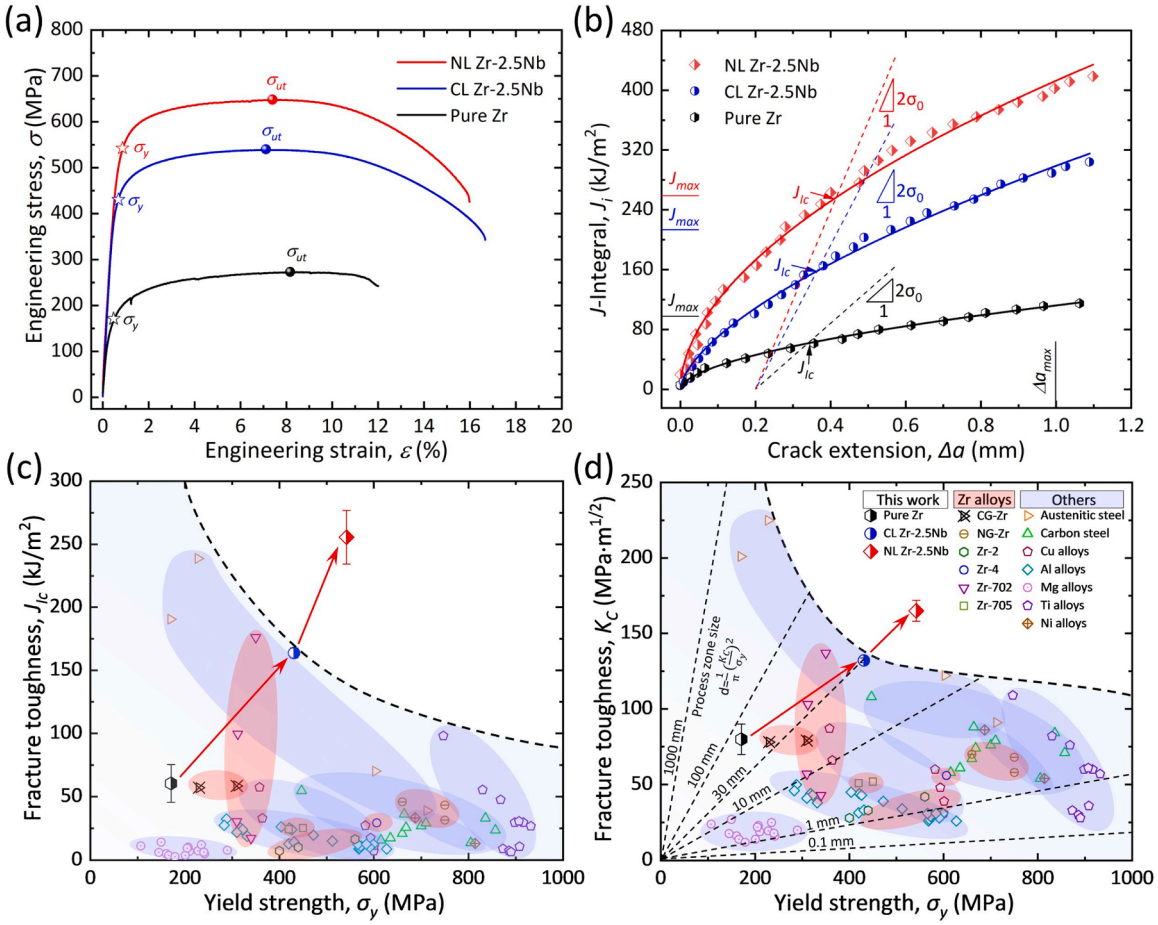

Fig. 2. Tensile and fracture properties of pure Zr, CL Zr-2.5Nb and NL Zr-2.5Nb. (a) Engineering stress-strain curves. (b) *J*-R curves for the fracture toughness tests. (c, d) Comparison of yield strength (σ_y) versus *J*-integral-based fracture toughness (J_{Ic}) in (c) and *K*-based fracture toughness (K_c) in (d) for NL Zr-2.5Nb to other alloys, including Zr alloys [25-29], austenitic steel [30], carbon steel [31], Cu alloys [32,33], Al alloys [34,35], Mg alloys [36-38], Ti alloys [39-41], and Ni alloys [42,43]. The J_{Ic} values of other metallic materials in (c) are back-calculated from their K_c values, $J_{Ic} = K_c^2/E'$.

Table 1
Uniaxial tensile and fracture toughness properties of pure Zr, CL Zr-2.5Nb and NL Zr-2.5Nb at room temperature.

Property	Pure Zr	CL Zr-2.5Nb	NL Zr-2.5Nb
0.2 %-offset yield strength, σ_y (MPa)	171	431	542
Ultimate tensile strength, σ_{ut} (MPa)	272	538	648
Effective yield stress, σ_0 (MPa)	222	485	595
Elongation to failure, ε_f (%)	12.01	16.67	15.98
J-integral at crack initiation, J_Q (kJ · m^{-2})	60.5 ± 14.9	163.7 ± 4.0	255.6 ± 21.3
Fracture toughness at crack initiation, K_Q (MPa · m$^{1/2}$)	79.9 ± 10.0	132.1 ± 1.6	165.0 ± 6.9
Crack growth *J*-integral at $\Delta a \sim 1.0$ mm, J_{SS} (kJ · m^{-2})	107.7 ± 14.7	284.6 ± 25.2	417.4 ± 47.3
Crack growth toughness at $\Delta a \sim 1.0$ mm, K_{SS} (MPa · m$^{1/2}$)	107.0 ± 7.4	174.1 ± 7.8	210.7 ± 11.9
Max *J*-integral, J_{max} (kJ · m^{-2})	97.7	213.4	261.8

thickness, and the flow stress, respectively. Based on the σ_0 of pure Zr, CL Zr-2.5Nb, and NL Zr-2.5Nb (Table 1), the calculated $10J_Q/\sigma_0$ values are 2.73 mm, 3.38 mm, and 4.29 mm, respectively. Both b_0 (~4.4 mm) and *B* (~5 mm) are larger than the required critical value $10J_Q/\sigma_0$ for the three types of Zr, indicating that their provisional J_Q can be regarded as an ASTM valid J_{Ic}. Therefore, the corresponding *K*-based fracture toughness values can be calculated using the standard mode-I *J*-*K* equivalence relationship, $K_{JIc} = (E' \cdot J_{Ic})^{1/2}$, where $E' = E$ (Young's modulus) in plane stress or $E/(1-\nu^2)$ in plane strain, ν is Poisson's ratio (see details in Supplementary Materials). The NL Zr-2.5Nb exhibits a *K*-based crack-initiation toughness (K_{JIc}) of 165.0 MPa·m$^{1/2}$, surpassing that of pure Zr (79.9 MPa·m$^{1/2}$) and CL Zr-2.5Nb (132.1 MPa·m$^{1/2}$) by 107 % and 25 %, respectively.

According to the comparison of yield strength (σ_y) and *J*-inegral-based fracture toughness (J_{Ic}) for NL Zr-2.5Nb to other alloys in Fig. 2 (c), it is evident that the J_{Ic} of NL Zr-2.5Nb exceeds that of most metallic materials, including Zr alloys (highlighted with a red background) and most other alloys (highlighted with a blue background) [25-43]. In addition, when further compare their *K*-based fracture toughness (K_C), as shown in Fig. 2 (d), the introduction of a hierarchical nanolayered structure enables the fracture toughness of our NL Zr-2.5Nb to surpass that of almost all reported Zr alloys, while reaching the exceptional strength-fracture toughness synergy.

3.3. Fracture behavior and failure mechanisms

To compare the fracture behavior of pure Zr, CL Zr-2.5Nb, and NL Zr-2.5Nb, SEM characterization was conducted to analyze their fracture surface morphologies, as shown in Fig. 3. Significant differences in fracture modes are observed among the various Zr samples. In the crack propagation region, pure Zr exhibits a typical semi-brittle fracture morphology characterized by numerous flat facets and only a few dimples (Fig. 3 (a, b)). The CL Zr-2.5Nb alloy also displays a similar semi-brittle fracture mode, but with more dimples present (Fig. 3 (c, d)). In contrast, the NL Zr-2.5Nb alloy displays a fully ductile fracture mode,

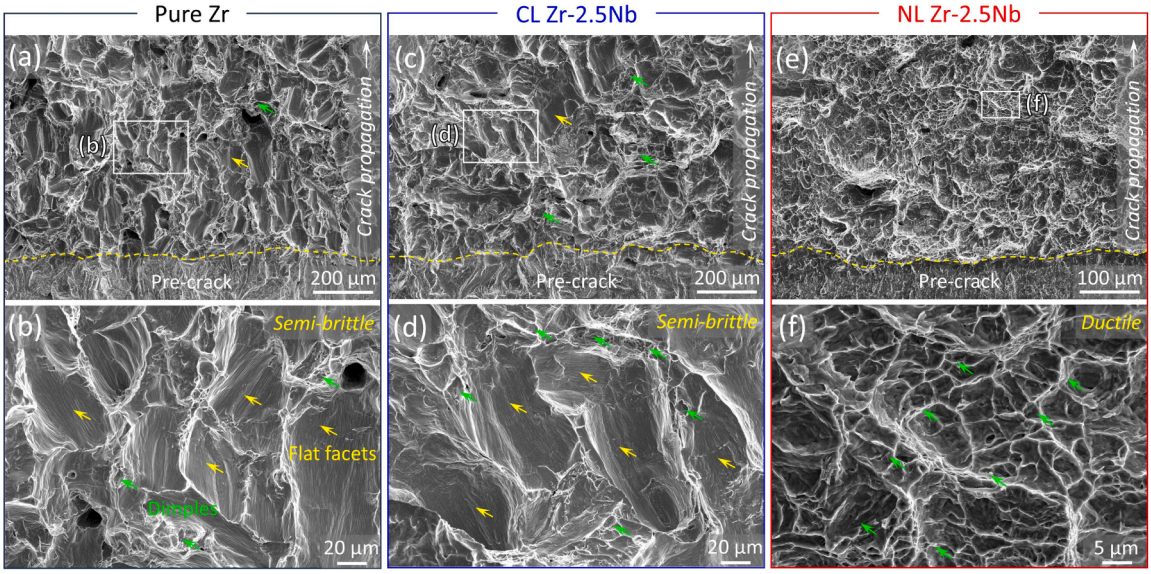

Fig. 3. Fracture surface in pure Zr, CL Zr-2.5Nb and NL Zr-2.5Nb SEB samples. (a, b) The crack propagation region of pure Zr exhibits an obvious semi-brittle fracture mode, characterized by numerous flat facets (indicated by yellow arrows) and a few dimples (green arrows). (c, d) The crack propagation region of CL-Zr-2.5Nb displays a similar semi-brittle fracture morphology, but with more dimples formed. (e, f) NL Zr-2.5Nb exhibits a completely ductile fracture, with a large number of dimples distributed throughout the entire crack propagation region.

with numerous dimples distributed throughout the crack propagation region (Fig. 3 (e, f)).

Based on the deformation morphologies on the pre-polished surface in pure Zr, it is evident that plastic deformation is primarily dominant by single and planar slip bands with preferred orientations within the grains (Fig. 4 (b)), leading to a limited and non-uniform plastic

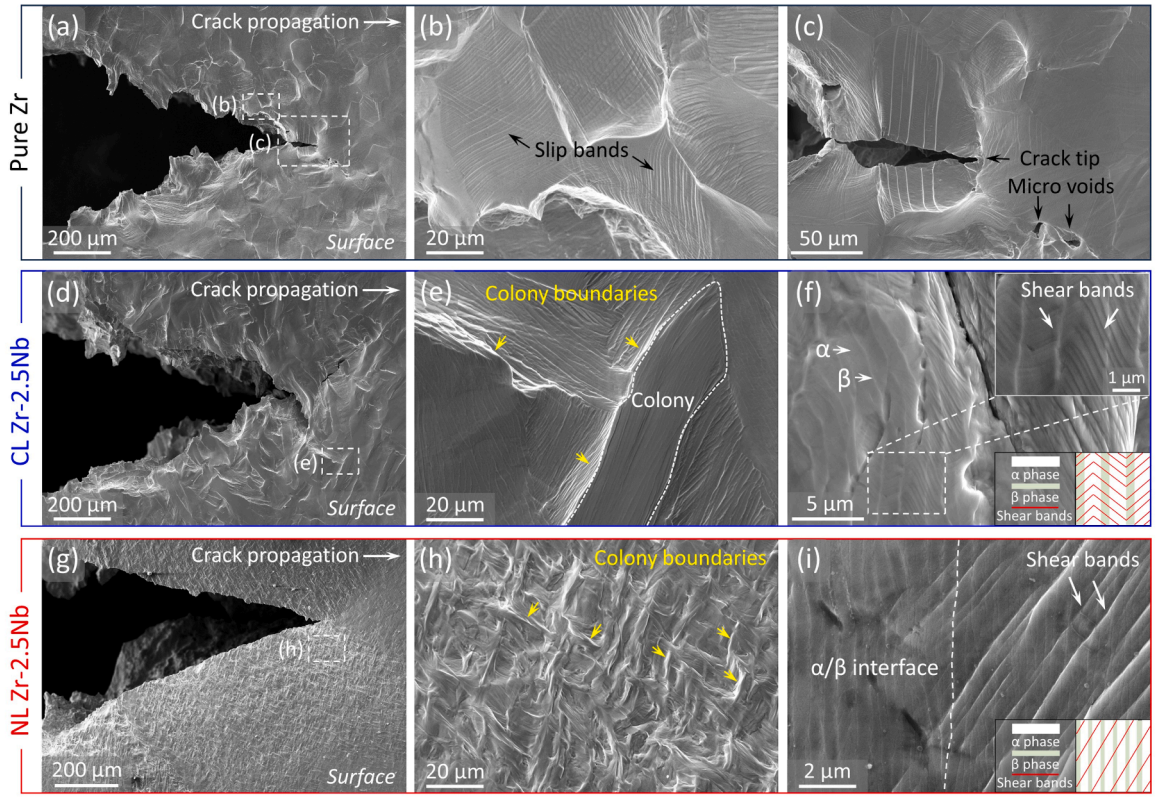

Fig. 4. Fracture and deformation behavior of pure Zr, CL Zr-2.5Nb, and NL Zr-2.5Nb on the surface, which closely represents the plane-stress condition. (a-b) SEM images showing evidence that a single slip mode is activated near the crack path of pure Zr inside a single grain. (c) Micro-voids are generated at the grain boundary ahead of the crack tip. (d, e) Non-uniform deformation occurs near the crack path in CL Zr-2.5Nb. (f) Multiple shear bands that traverse multiple α/β-Zr lamellae are generated in CL Zr-2.5Nb to disperse and alleviate stress concentration at the crack tip. (g, h) NL Zr-2.5Nb displays uniform and severe plastic deformation in the vicinity of crack path, as verified by the obviously deformed colonies in (h). (i) Shear bands are also activated in NL Zr-2.5Nb. The colony boundaries are indicated by the yellow arrows in (e) and (h).

deformation capacity. Moreover, micro-voids are more likely to generate at grain boundaries (GBs) (Fig. 4 (c)), which can lead to the rapid crack propagation over a long distance along large-scale GBs. As a result, pure Zr exhibits a relatively low fracture resistance. The CL Zr-2.5Nb sample also displays a similar slight and non-uniform plastic deformation morphology to pure Zr near the crack path, as shown in Fig. 4 (d-f).

By contrast, plastic deformation near the crack path was more significant and uniform in NL Zr-2.5Nb, as shown in Fig. 4 (g-i). In addition, no significant void or crack-like damage was observed within the plastic zone ahead of the crack tip (Fig. 4 (h)). Thus, these forms of severe and uniform deformation ahead of the crack tip can significantly hinder the crack propagation under plane-stress condition in NL Zr-2.5Nb.

To investigate the underlying failure mechanisms of the various Zr samples under plane-strain conditions, some SEB specimens with a crack extension of ~1 mm were sliced in two halves, and their cross-sections were polished for SEM and EBSD characterizations, as shown in Fig. 5. Based on the crack-path morphologies on the mid-plane of pure Zr (Fig. 5 (a)), CL Zr-2.5Nb (Fig. 5 (e)), and NL Zr-2.5Nb (Fig. 5 (i)), all the main cracks appear to be relatively straight, especially in the case of NL Zr-2.5Nb. This straight crack path satisfies the requirements of ASTM E1820 standard [22]. Notably, in contrast to the sharp crack tip in pure Zr and CL Zr-2.5Nb samples, the NL Zr-2.5Nb develops a blunted crack tip (Fig. 5 (i)), which is a sign of its superior crack resistance. Additionally, the crack can locally deflect along the α/β-Zr interfaces (Fig. 5 (j)), further hindering subsequent crack propagation in the NL Zr-2.5Nb.

The EBSD IPF maps (Fig. 5 (c, g, k)) are plotted to examine the crystalline orientation distribution near the crack path of the three SEB samples. The scanning step size for pure Zr, CL Zr-2.5Nb and NL Zr-2.5Nb is 0.3 μm, 0.2 μm and 0.2 μm, respectively. The corresponding kernel average misorientation (KAM) maps (Fig. 5 (d, h, l)) with a kernel size of 5 × 5 and a maximum angle of 5° are presented to qualitatively compare the extent of plastic deformation. In both CL Zr-2.5Nb and NL Zr-2.5Nb, the high KAM value extends over a wide region around the crack path and is distributed homogeneously inside the colonies, as opposed to being localized near the crack and a few grain boundaries as seen in pure Zr. Additionally, NL Zr-2.5Nb displays a higher KAM value compared to CL Zr-2.5Nb (Fig. 5 (l)). The substantial capacity for plastic deformation ahead of the crack tip in NL Zr-2.5Nb therefore effectively blunts the crack tip. According to the corresponding EBSD pole figures (Fig. S2), the orientation distribution of α-Zr colonies in both CL Zr-2.5Nb and NL Zr-2.5Nb samples is not significantly different, which is further indicating that there are no significant texture differences between them that would cause different slip or twinning systems to be activated and no bias from texture that would favor one mode over another. The nearly random orientation of α-Zr colonies in NL Zr-2.5Nb is further demonstrated in Fig. 1 (c-e).

3.4. Deformation mechanisms ahead of the crack tip

To further investigate the micro-mechanisms that contribute to the severe and uniform plastic deformation occuring at the crack tip, we performed an in-depth TEM analysis of dislocation structures, including <a> dislocations and <c+a> dislocations, in the three types of Zr samples studied here.

Within the plastic zone ahead of the crack tip in pure Zr, numerous <a>-type dislocations were observed (Fig. S3(a-c)). These <a> dislocations are associated with slip on three equivalent prismatic planes (see Supplementary Mateirials). In contrast, from Fig. 6 (a), we observe only a small number of <c+a> dislocations using $\vec{g} = 0002$, and most of them were emitted from GB, as evidenced by the "bow-out" shape of <c+a> dislocations at the GB. Notably, many <c+a> dislocations in

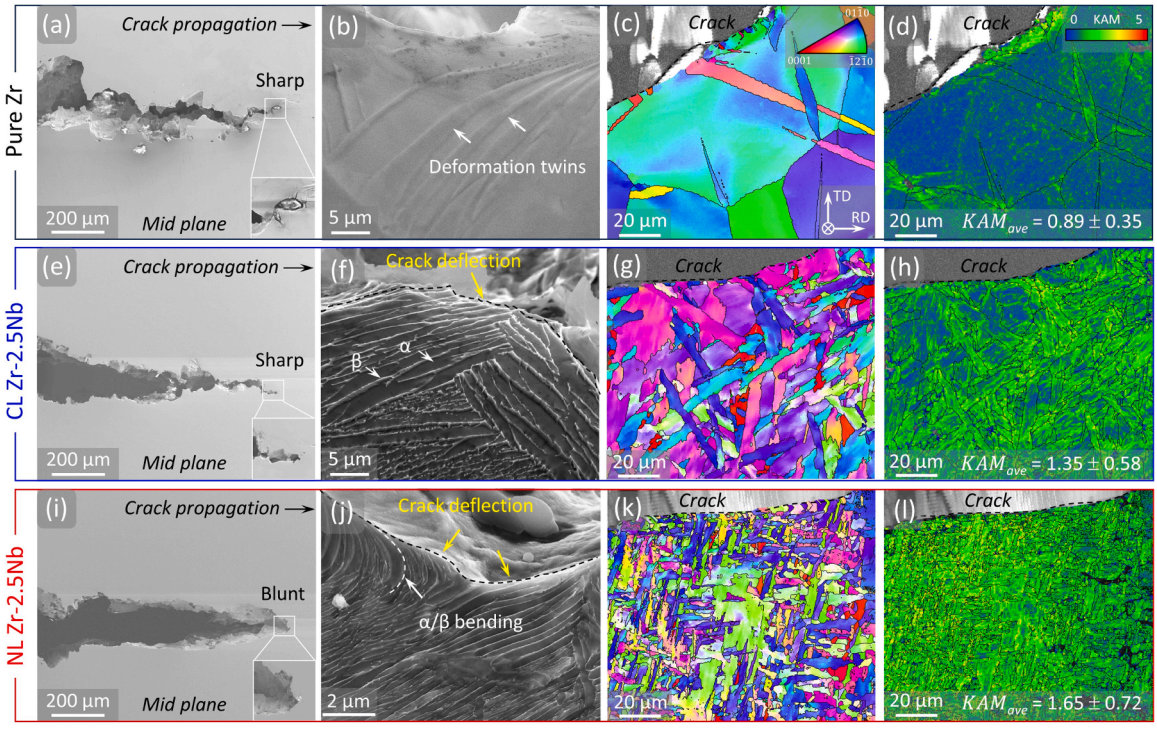

Fig. 5. Fracture morphologies and deformation mechanisms in pure Zr, CL Zr-2.5Nb and NL Zr-2.5Nb on the mid-plane, which closely represents the plane-strain condition. (a-d) Fracture and deformation morphologies of pure Zr. (a) SEM image of the crack profile showing a discernible sharp crack-tip. (b) A few deformation twins are activated. (c) Orientation map and corresponding (d) KAM map showing slight plastic deformation near the crack path. (e) CL Zr-2.5Nb also exhibits a sharp crack-tip. (f) The main crack is deflected along the α/β interfaces of CL-Zr-2.5Nb. (g, h) Significant plastic deformation and a high average KAM value are observed in CL Zr-2.5Nb. (i) NL Zr-2.5Nb displays a significantly blunted crack-tip. (j) Crack deflection along α/β interfaces also occurs in NL Zr-2.5Nb, and the α/β-Zr layers are bent near the crack path. (k, l) More severe deformation and a higher average KAM value are exhibited in NL Zr-2.5Nb. Orientation maps in (c), (g), and (k) use the same inverse pole figure key in (c) and KAM maps use the same legend as in (d).

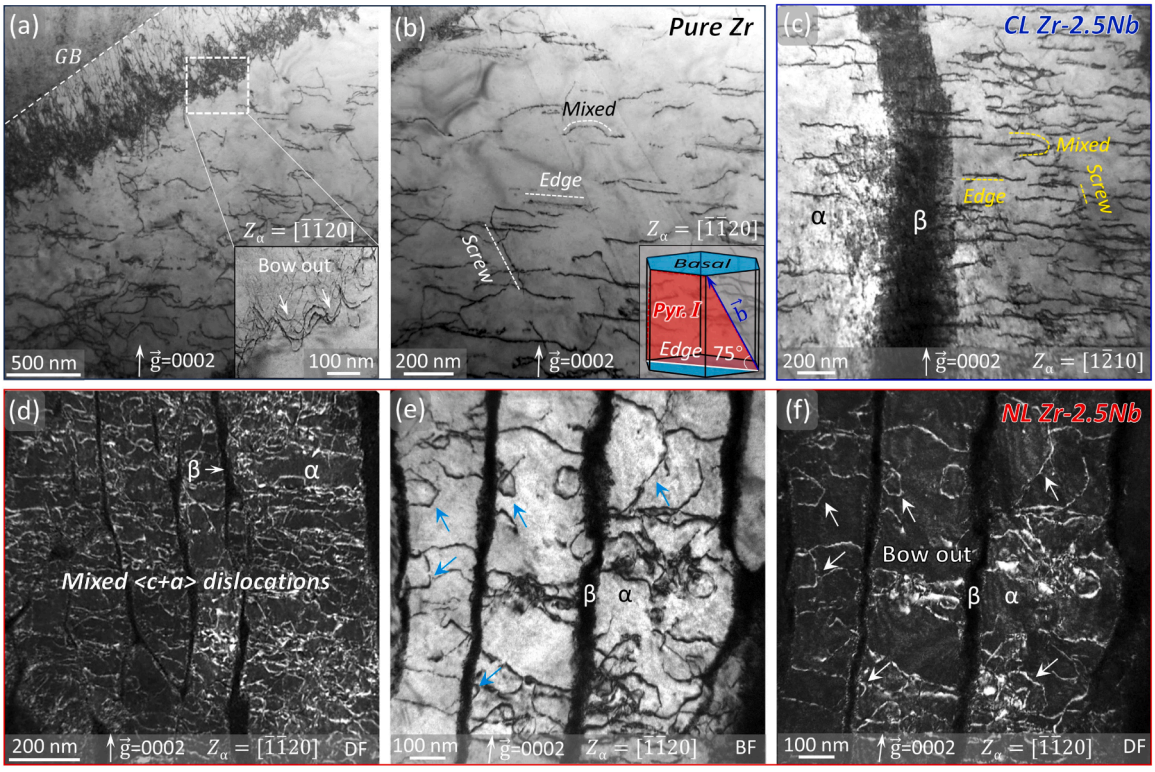

Fig. 6. TEM characterization of dislocations ahead of the crack tip (within the plastic zone) in pure Zr, CL Zr-2.5Nb and NL Zr-2.5Nb. (a) A Bright-field (BF) TEM image under $\vec{g} = 0002$ showing <c+a> dislocations being emitted from GBs in pure Zr. (b) Most of <c+a> dislocations are preferentially aligned along the intersection line of first-order pyramidal plane and basal plane in pure Zr; thus, they are near edge components, as verified by the inserted schematic diagram. (c) A BF TEM image showing more <c+a> dislocations are activated, and most of them are edge-character in CL Zr-2.5Nb. (d-f) Dislocation morphology of NL Zr-2.5Nb. (d) A dark-field (DF) TEM image showing a much higher density of mixed <c+a> dislocations with curved morphologies are activated. (e) A BF TEM image and (f) the corresponding DF TEM image showing these <c+a> dislocations nucleate from α/β interfaces, as verified by their bow-out shape.

pure Zr are relatively stright and parallel to the basal plane, indicating that they possess a large edge component due to the angle of 75° between the dislocation line and its Burgers vector (Fig. 6 (b)). Only a few straight dislocations exhibit screw character, and the remaining dislocations are mixed segments with curved morphologies (Fig. 6 (b)).

In CL Zr-2.5Nb, the presence of the α/β-Zr interfaces affected the dislocation structures within the α-Zr lamellae. Although prismatic <a> slip within α-Zr layers still carried most of the plastic deformation ahead of the crack tip (Fig. S3(d-f)), there was a heightened density of <c+a> dislocations compared to that within the pure α-Zr sample (Fig. 6 (c)), which can lead to more plasticity along the <c>-axis. Numerous <c+a> dislocations still exhibited nearly edge segments aligned parallel to basal plane. It has been confirmed that these <c+a> edge dislocations slipped on multiple first-order pyramidal planes (see details in Fig. S4 and Supplementary Text), which is an obvious sign of enhanced activity of <c+a> dislocations ahead of the crack tip in CL Zr-2.5Nb.

With the further increase in the density of α/β-Zr interfaces in the NL Zr-2.5Nb, the density of both <a> dislocations (Fig. S3(g-i)) and <c+a> dislocations (Fig. 6 (d-f)) increase. According to the dark-field (DF) TEM image in Fig. 6 (d), a much higher density of <c+a> dislocations can be observed. Further, based on their distribution, these <c+a> dislocations were activated homogeneously within the α-Zr layers. In contrast to the <c+a> dislocations with large edge components in pure Zr and CL Zr-2.5Nb, the majority of <c+a> dislocations are mixed-character segments with curved morphologies in NL Zr-2.5Nb (Fig. 6 (d)). It was also inferred that these mixed <c+a> segments in NL Zr-2.5Nb slipped on different first-order <c+a> pyramidal planes (Fig. S5 and Supplementary Text). More importantly, in a bright-field (BF) TEM image (Fig. 6 (e)) and its corresponding DF TEM image (Fig. 6 (f)), the "bow-out" shape of <c+a> dislocations at α/β-Zr interfaces were also captured. This observation suggests that high density of α/β-Zr interfaces serve as sources for the emission of numerous <c+a> dislocations at the crack tip.

In addition to dislocation slip, the generation of mutiple intra-colony deformation twins was also observed ahead of the crack tip in NL Zr-2.5Nb (Fig. 7 and Fig. S6). The detailed structure of four twins labelled 1, 2, 3, and 4 is revealed by BF and DF TEM images in Fig. 7 and Fig. S7. By analyzing SADPs of the matrix and twinning (Fig. 7 (c, d) and Fig. S7(d-g)), all four twins are confirmed $\{1\bar{1}02\}\langle\bar{1}101\rangle$ (T1) extension twins. Twin-1 and twin-4, as well as twin-2 and twin-3, correspond to two distinct variants with twinning planes of $(\bar{1}102)$ and $(1\bar{1}02)$, respectively. These twins propagated across multiple α/β-Zr interfaces. We further observe that the α/β-Zr interfaces became preferential nucleation sites for twins, as indicated by yellow arrows in Fig. 7 (f). This observation demonstrates that numerous α/β-Zr interfaces can promote, rather than suppress, the activation of deformation twins. Moreover, as outlined by blue dashed lines in Fig. 7 (a, e), distinctive step-like twin boundaries were formed, which could be attributed to the presence of α/β-Zr interfaces.

4. Discussion

4.1. Enhanced <c+a> dislocation activity for crack-tip blunting

In HCP metals, enhancing the overall ability for uniform deformation ahead of the crack tip is essential for improving fracture resistance [44-46]. This is usually achieved by promoting the activation of dislocation slip and deformation twinning. However, in Zr, it is challenging to homogeneously activate these mechanisms. They accommodate strains only in distinct directions and exhibit substantial differences

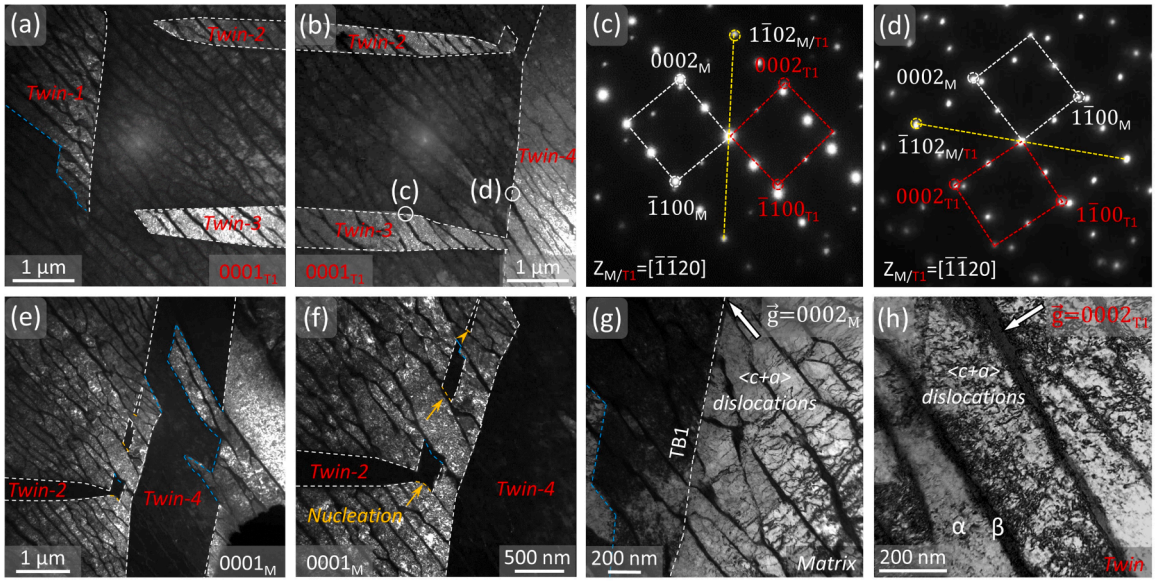

Fig. 7. TEM characterization of deformation twins ahead of the crack tip in NL Zr-2.5Nb. (a, b) DF TEM images showing several deformation twins that have propagated through multiple α/β layers. (c, d) SADPs from the white circles in (b) showing that these twins are two variants of {1$\bar{1}$02}-type (T1) twins. (e, f) DF TEM images showing the T1 twins likely nucleated from the α/β interfaces, as suggested by the yellow dashed lines. They terminate at the phase boundaries, as indicated by blue dashed lines. The BF TEM images under $\vec{g}$ = 0002 showing numerous <c+a> dislocations have activated in both (g) the matrix and (h) twin domains.

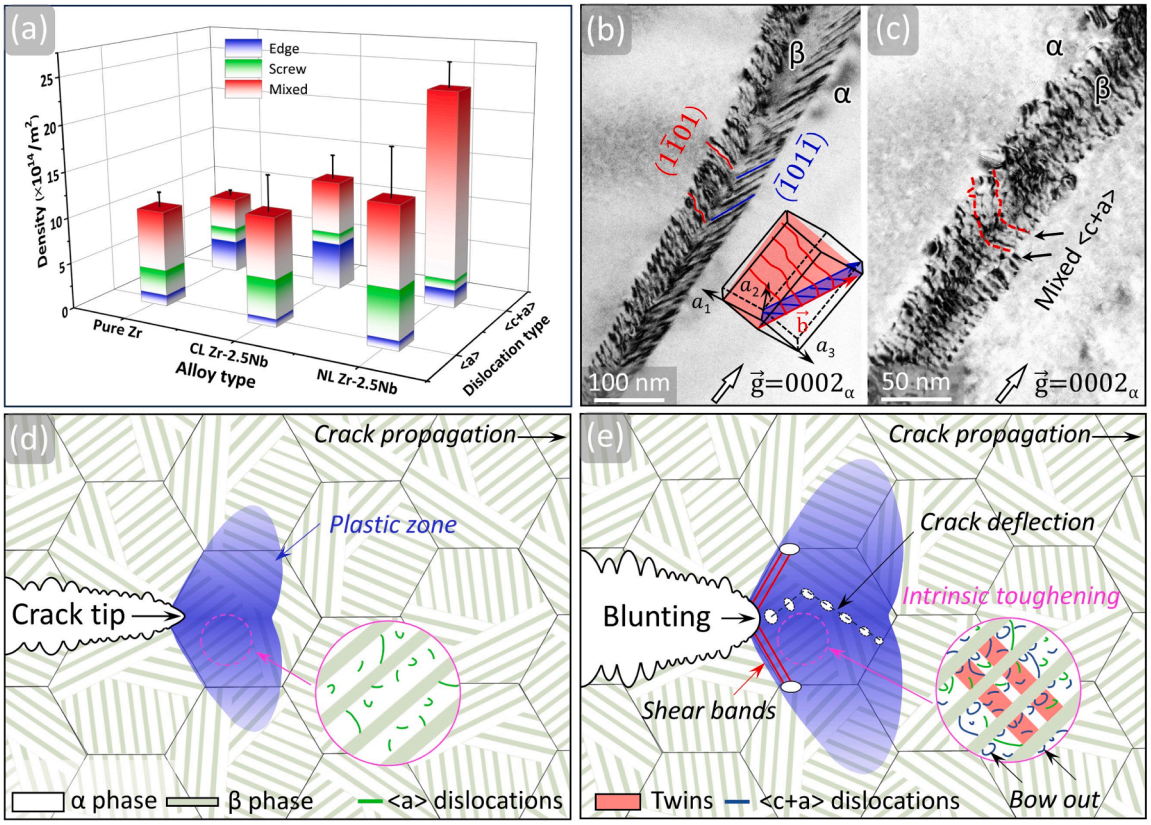

Fig. 8. Intrinsic toughening mechanisms of NL Zr-2.5Nb. (a) 3D statistical plot depicting the density variations of different types of dislocations, including <a> edge/screw/mixed and <c+a> edge/screw/mixed, in pure Zr, CL Zr-2.5Nb and NL Zr-2.5Nb. Numerous <c+a> interfacial dislocations are seen in NL Zr-2.5Nb using $\vec{g}$ = 0002 under a zone axis of (b) $[1\bar{2}10]_\alpha$ and (c) $[01\bar{1}0]_\alpha$. Most of them are located on different first-order pyramidal planes, which are depicted by the inserted schematic in (b). A portion of the <c+a> interfacial dislocations in (c) are mixed with curved lines. (d, e) Schematics displaying the intrinsic toughening process of NL Zr-2.5Nb during the crack-initiation stage. (d) A small number of prismatic <a> dislocations are firstly activated inside the α-Zr lamellae ahead of the crack tip. (e) Deformation twins and a high density of <c+a> dislocations are subsequently generated from the α/β interfaces to blunt the crack tip.

among their activation stresses [11,15]. Therefore, to improve fracture resistance, it becomes critically important to reduce these differences in the propensity of these deformation modes to activate. As we demonstrate in the context of our multi-scale fracture toughness investigation, pure Zr clearly does not achieved this goal. As shown in Fig. 8 (a), many prismatic <a> dislocations but only a significantly lower density of <c+a> dislocations were activated. This can be expected since <c+a> slip have a much higher CRSS than <a> slip [15]. Further, most of the <c+a> dislocations are low-mobility edge components due to high lattice friction [16] or partial non-planar dissociation onto the basal plane [18], which further reduces their self-multiplication ability [19]. Although the GBs in pure Zr were observed to serve as <c+a> dislocation sources (Fig. 4 (a)), the fraction of GBs in typical coarse-grained pure Zr is still too low to activate a sufficient number of <c+a> dislocations. Limited activity of <c+a> dislocations restricts plastic accommodation of deformation in the <c>-axis of the Zr crystals. Eventually, the non-uniform deformation ahead of the crack tip leads to a rapid crack extension.

In contrast, the introduction of α/β interfaces in layered Zr-2.5Nb effectively improved the capacity for uniform deformation ahead of the crack tip. Not only were more <a> dislocations activated (Fig. 8 (a)) to accommodate ample <a>-axis plasticity, but the inherent low activity of <c+a> slip in Zr-based materials has been overcome [47]. A greater number of <c+a> dislocations, gliding on multiple first-order pyramidal planes, were activated ahead of the crack tip in the NL Zr-2.5Nb (Fig. 8 (a) and Fig. S5). Particularly, the average density of <c+a> dislocations in NL Zr-2.5Nb even exceeds that of <a> dislocations, making <c+a> slip the predominant deformation mode ahead of the crack tip (Fig. 8 (a)).

It is uncommon to activate such a high density of <c+a> dislocations in an HCP Zr-based material [47]. The Nb content within α-Zr phase in Zr-2.5Nb is ~0.5 wt.% [23]. The diffusion of Nb in the α-Zr phase primarily depends on the cooling time, with mechanical deformation processes having minimal impact on Nb diffusion. Therefore, the residual Nb content in the α-Zr of both CL Zr-2.5Nb and NL Zr-2.5Nb is the same and consistent with their common air-cooling rates. Notably, the presence of Nb within the α-Zr phase has been shown to increase the CRSS for <c+a> slip [23], which means increases in the activation stress for forming <c+a> dislocations in the α-Zr lamellae over pure α-Zr can be expected. Close characterization of the α/β interfaces in NL Zr-2.5Nb using $\vec{g} = 0002$ shows numerous stored <c+a> dislocations (Fig. 8 (b-c)). In Fig. 8 (b), two arrays of <c+a> dislocations can be seen located on either side of the α/β interface, as outlined by the colored lines. Based on the HCP unit cell schematic, the <c+a> dislocations from one array, highlighted by blue lines, are nearly parallel to the trace of the $(\bar{1}01\bar{1})$ plane, indicating that they are located on the $(\bar{1}01\bar{1})$ plane. The <c+a> dislocations from the other array outlined in red lie on the $(1\bar{1}01)$ plane and possess a Burgers vector of $\vec{b} = 1/3[\bar{2}113]$. These are like the α/β interfacial <c+a> dislocations reported in an earlier study on duplex-phase layered Zr-2.5Nb [48]. These interfacial dislocations are densely packed, spaced only 5 – 10 nm apart, which can provide numerous sources for <c+a> dislocations on at least two orientations of first-order pyramidal planes and in this way, contribute to the greater plastic capacity ahead of the crack tip in NL Zr-2.5Nb. Therefore, high-density α/β-Zr interfaces promoted the activation of <c+a> dislocations through the following mechanisms: (1) The steps at the α/β-Zr interfaces (Fig. 1 (h, i)) may become the nucleation sites for <c+a> dislocations; (2) The dense pre-existing interfacial <c+a> dislocations at the α/β-Zr interfaces can serve as sources to emit numerous <c+a> dislocations. This source-like behavior is evidenced by the "bow-out" shape of the <c+a> dislocations at α/β-Zr interfaces, see Fig. 6 (e, f).

In addition, unlike in pure Zr and CL Zr-2.5Nb, where most <c+a> dislocations are near-edge character, in NL Zr-2.5Nb, the <c+a> dislocations are primarily mixed character (Fig. 8 (a)). Yet the density of edge component is still higher than that of the screw components (Fig. 8 (a)), which indicates that dislocations in NL Zr-2.5Nb still retain the edge/screw mobility difference expected of <c+a> dislocations in Zr. We suspect that most <c+a> dislocations bowing out from sources within the α/β interfaces (Fig. 8 (c)) have preserved their curved shape in the α-Zr lamellae of NL Zr-2.5Nb. In contrast, in the pure Zr and CL Zr-2.5Nb samples, the lack of dislocation sources results in these <c+a> dislocations predominantly gliding within the α-Zr phase and leaving behind edge segments with limited mobility. Thus, higher <c+a> dislocation density results more from frequent emission of dislocations from the α/β interfaces and less from line extension from dislocation propagation through the layers. In this way, introduction of numerous α/β interfaces in NL Zr-2.5Nb significantly enhanced the activity of <c+a> dislocations, providing sufficient <c>-axis plasticity and blunting of the crack tip compared to pure Zr and CL Zr-2.5Nb.

4.2. Deformation twinning for crack-tip blunting

In addition to <c+a> slip, deformation twinning is another important deformation mode that accommodates <c>-axis deformation in HCP Zr and can contribute to achieving uniform plastic deformation ahead of the crack tip [24,47]. However, abundant twinning in any of these Zr-based material would not be anticipated at room temperature for two reasons. The CRSS required for twin growth (~102 MPa for T1 at room temperature) is much higher than that for activating prismatic <a> slip in Zr [11], leading to a typically low volume fractions of deformation twins at room temperature [12]. Also, second phases can further hinder twin growth. For duplex nanostructured metals with a high density of precipitates, for instance, deformation twins must engulf or bypass the precipitates in order to grow [49]. Likewise, in NL Zr-2.5Nb, it would be expected that the growth of deformation twins within multiple α-Zr lamellae would face difficulties when bypassing multiple β-Zr layers, each with in-plane micron-scale dimensions. Therefore, in the present study, it is suspected that multiple twins are fostered via combination of high stresses ahead of the crack tip and rampant twin nucleation from the numerous α/β interfaces.

Regarding nucleation, Fig. 7 (f) confirms that multiple twins have nucleated near or at the α/β interfaces. Previously studies have reported that the pile-up of <a> dislocations at α/β interfaces can lead to the nucleation of deformation twins [50,51]. This pile-up has also been captured in the NL Zr-2.5Nb [21]. Pyramidal <c+a> interfacial dislocations may also transform into twinning dislocations to assist twinning nucleation [51]. After nucleation, these twins propagate by "hopping" across the ultra-thin β-Zr lamellae (Fig. 7), a phenomenon consistent with earlier observations [52]. During twinning growth, when the twin tip encounters the α/β interfaces, the nanoscale β-Zr lamellae is sufficiently thin to transmit high stresses from the impingement site into the adjacent α-Zr layer. These stresses can trigger the re-nucleation of a new twin at the opposite α/β interface [52]. In these ways, α/β interfaces and ultra-thin β layers in NL Zr-2.5Nb promote the activation and growth of multiple deformation twins, which provided extra <c>-axis plasticity to blunt the crack tip. In addition, the T1 twins are domains that reorient the α-Zr lamellae from a hard orientation into a more favourable soft orientation for <c+a> dislocation slip. Compared to the matrix (Fig. 7 (g)), this reorientation leads to the activation of a higher density of <c+a> dislocations inside the α_{T1} layers within twinning (Fig. 7 (h)), further facilitating <c>-axis deformation.

4.3. Crack propagation process

Fig. 8 (d, e) illustrates the process of crack propagation in NL Zr-2.5Nb based on all aforementioned toughening mechanisms. In the early stage of crack initiation (Fig. 8 (d)), the plastic zone ahead of the crack tip is small [45], and the predominant plastic deformation mechanism inside the zone is prismatic <a> slip. With increasing applied stress at the crack tip, a high density of α/β interfaces promotes the activation of numerous <c+a> dislocations and deformation twins

to accommodate <c>-axis plasticity, enlarging the plastic zone (Fig. 8 (e)). This enhanced uniform deformation capacity provided sufficiently large intrinsic toughening effect to blunt the crack tip. These mechanisms are key to the superior crack-initiation toughness. With further increases in stress, the main crack then propagates forward. At this stage, the relatively weak α/β interfaces locally deflect the main crack along α/β interfaces (Fig. 8 (e) and Fig. 5 (j)), which serves as a crack-growth toughening mechanism.

5. Conclusions

In summary, we show that an exceptionally high fracture resistance at ambient temperature is possible in a Zr-Nb alloy with the introduction of a hierarchical nanolayered (NL) microstructure. Comparisons to pure Zr and CL Zr-2.5Nb, high-density α/β duplex-phase interfaces in the NL Zr-2.5Nb alloy are responsible for its unprecedented fracture toughness. We find that the α/β interfaces promote an unusually uniform and dense plastic deformation ahead of the crack tip, which contrasts with the non-uniform, highly anisotropic, and insufficient crack-tip deformation that occurs in the traditional Zr alloys. We show that α/β interfaces promote significant activity of <c+a> dislocations and deformation twins, which are mechanisms that usually do not occur in Zr at room temperature. The exceptional fracture resistance of NL Zr-2.5Nb thus possesses the potential to effectively hinder the propagation of hydride-induced cracks during service in nuclear reactors. Advantageously this structural design strategy can be extended to other two-phase HCP alloy systems, such as titanium alloys, which need boosts in their damage tolerance for safety-critical applications.

CRediT authorship contribution statement

Xiao-Wei Zou: Writing – original draft. **Irene J. Beyerlein:** Writing – review & editing. **Wei-Zhong Han:** Writing – review & editing, Conceptualization.

Declaration of competing interest

The authors declare no competing financial interests.

Acknowledgments

This research was supported by the National Natural Science Foundation of China (Grant Nos. 51922082 and 51971170). X.W. Zou acknowledges Y.B. Qin, J.W. Zhang, X.Q. Wang, X.L. Song and S.H. Gao for their assistance on sample preparation.

Supplementary materials

Supplementary material associated with this article can be found, in the online version, at doi:10.1016/j.actamat.2024.120300.

References

[1] R.A. Holt, In-reactor deformation of cold-worked Zr-2.5Nb pressure tubes, J. Nucl. Mater. 372 (2008) 182–214.
[2] L. Balogh, D.W. Brown, P. Mosbrucker, F. Long, M.R. Daymond, Dislocation structure evolution induced by irradiation and plastic deformation in the Zr-2.5Nb nuclear structural material determined by neutron diffraction line profile analysis, Acta Mater. 60 (2012) 5567–5577.
[3] S.M. Liu, I.J. Beyerlein, W.Z. Han, Two-dimensional vacancy platelets as precursors for basal dislocation loops in hexagonal zirconium, Nat. Commun. 11 (2020) 5766.
[4] S.M. Liu, A. Ishii, S.B. Mi, S. Ogata, J. Li, W.Z. Han, Dislocation-mediated hydride precipitation in zirconium, Small 18 (2022) 2105881.
[5] Y.J. Jia, W.Z. Han, Mechanisms of hydride nucleation, growth, reorientation and embrittlement in zirconium: A review, Materials 16 (2023) 2419.
[6] L.A. Simpson, C.D. Cann, Fracture toughness of zirconium hydride and its influence on the crack resistance of zirconium alloys, J. Nucl. Mater. 87 (1979) 303–316.
[7] M. Kuroda, K. Yoshioka, S. Yamanaka, H. Anada, F. Nagase, H. Uetsuka, Influence of precipitated hydride on the fracture behavior of zircaloy fuel cladding tube, J. Nucl. Sci. Technol. 37 (2000) 670–675.
[8] R.O. Ritchie, The conflicts between strength and toughness, Nat. Mater. 10 (2011) 817–822.
[9] R.O. Ritchie, Mechanisms of fatigue crack-propagation in metals, ceramics and composites: Role of crack tip shielding, Mater. Sci. Eng. A 103 (1988) 15–28.
[10] M.H. Yoo, Slip, twinning, and fracture in hexagonal close-packed metals, Metall. Trans. A 12 (1981) 409.
[11] M.A. Kumar, I.J. Beyerlein, C.N. Tome, Effect of local stress fields on twin characteristics in HCP metals, Acta Mater. 116 (2016) 143–154.
[12] J.W. Zhang, J.X. Wang, X.W. Zou, I.J. Beyerlein, W.Z. Han, Texture evolution and temperature-dependent deformation modes in ambient- and cryogenic-rolled nanolayered Zr-2.5Nb, Acta Mater. 234 (2022) 118023.
[13] R. Von Mises, Mechanik der plastischen Formaenderung von Kristallen, Z. Angew. Math. Mech. 8 (1928) 161–185.
[14] G.I. Taylor, Plastic strain in metals, J. Inst. Metals 62 (1938) 307–324.
[15] A. Akhtar, Compression of zirconium single crystals parallel to the c-axis, J. Nucl. Mater. 47 (1973) 79–86.
[16] T. Soyez, D. Caillard, F. Onimus, E. Clouet, Mobility of <c + a>dislocations in zirconium, Acta Mater. 197 (2020) 97–109.
[17] Y.Q. Bu, Z.M. Li, J.B. Liu, H.T. Wang, D. Raabe, W. Yang, Nonbasal slip systems enable a strong and ductile hexagonal-close-packed high-entropy phase, Phys. Rev. Lett. 122 (2019) 075502.
[18] Z. Wu, B. Yin, W.A. Curtin, Energetics of dislocation transformations in hcp metals, Acta Mater. 119 (2016) 203–217.
[19] Y. Lu, Y.H. Zhang, E. Ma, W.Z. Han, Relative mobility of screw versus edge dislocations controls the ductile-to-brittle transition in metals, Proc. Natl. Acad. Sci. U.S.A. 118 (2021) e21105961182021.
[20] Z.X. Wu, R. Ahmad, B.L. Yin, S. Sandlöbes, W.A. Curtin, Z.X. Wu, Mechanistic origin and prediction of enhanced ductility in magnesium alloys, Science 359 (2018) 447–452.
[21] J.W. Zhang, I.J. Beyerlein, W.Z. Han, Hierarchical 3D nanolayered duplex-phase Zr with high strength, strain hardening, and ductility, Phys. Rev. Lett. 122 (2019) 255501.
[22] ASTM International, E1820-17a Standard Test Method for Measurement of Fracture Toughness, ASTM International, 2017.
[23] S. Cai, M.R. Daymond, R.A. Holt, Deformation of high β-phase fraction Zr-Nb alloys at room temperature, Acta Mater. 60 (2012) 3355–3369.
[24] X.H. Lin, W.Z. Han, Achieving strength-ductility synergy in zirconium via ultra-dense twin-twin networks, Acta Mater. 269 (2024) 119825.
[25] M. Li, D.F. Guo, T.Y. Ma, G.S. Zhang, Y.D. Shi, X.Y. Zhang, High fracture toughness in a hierarchical nanostructured zirconium, Mater. Sci. Eng. A 606 (2014) 330–333.
[26] S. Goel, N. Kumar, D. Fuloria, R. Jayaganthan, I.V. Singh, D. Srivastava, G.K. Dey, N. Saibaba, Evaluating fracture toughness of rolled zircaloy-2 at different temperatures using XFEM, J. Mater. Eng. Perform. 25 (2016) 4046–4058.
[27] D.F. Guo, Y.D. Zhao, J.T. Li, K.F. Li, G.S. Zhang, M. Li, B.N. Wei, Q. Zhang, X.H. Li, X.Y. Zhang, Enhancing fracture toughness of fine-grained Zr via forming nanoscale defect structures, J. Alloys Compd. 729 (2017) 89–94.
[28] J.A. Wang, Fracture toughness evaluation for Zr-4 clad tubing structure with pellet inserts, Theor. Appl. Fract. Mech. 108 (2020) 102657.
[29] S. Zeng, G.Q. You, F.J. Yao, J.C. Luo, X. Tong, Effect of bonding temperature on the microstructure and mechanical properties of the diffusion-bonded joints of Zr705 alloy, Mater. Sci. Eng. A 804 (2021) 140782.
[30] X.R. Liu, H. Feng, J. Wang, X.F. Chen, P. Jiang, F.P. Yuan, H.B. Li, E. Ma, X.L. Wu, Mechanical property comparisons between CrCoNi medium-entropy alloy and 316 stainless steels, J. Mater. Sci. Technol. 108 (2022) 256–269.
[31] L. Liu, Q. Yu, Z. Wang, J. Ell, M.X. Huang, R.O. Ritchie, Making ultrastrong steel tough by grain-boundary delamination, Science 368 (2020) 1347–1352.
[32] S.D. Qu, Z.S. You, R.C. Gu, Y. Jiang, J.T. Wang, Fracture toughness anisotropy of ultrafine-grained pure copper processed by equal channel angular pressing, Mater. Sci. Eng. A 782 (2020) 139260.
[33] E.W. Qin, L. Lu, N.R. Tao, K. Lu, Enhanced fracture toughness of bulk nanocrystalline Cu with embedded nanoscale twins, Scr. Mater. 60 (2009) 539–542.
[34] M.Y. Yu, Y.A. Zhang, X.W. Li, K. Wen, B.Q. Xiong, Z.H. Li, L.Z. Yan, H.W. Yan, H. W. Liu, Y.A. Li, Effect of recrystallization on plasticity, fracture toughness and stress corrosion cracking of a high-alloying Al-Zn-Mg-Cu alloy, Mater. Lett. 275 (2020) 128074.
[35] N. Kamp, I. Sinclair, M.J. Starink, Toughness-strength relations in the overaged 7449 Al-based alloy, Metall. Mater. Trans. A 33 (2002) 1125–1136.
[36] H. Somekawa, T. Mukai, Fracture toughness in Mg–Al–Zn alloy processed by equal-channel-angular extrusion, Scr. Mater. 54 (2006) 633–638.
[37] W.C. Liu, L.K. Jiang, L. Cao, J. Mei, G.H. Wu, S. Zhang, L. Xiao, S.H. Wang, W. J. Ding, Fatigue behavior and plane-strain fracture toughness of sand-cast Mg–10Gd–3Y–0.5Zr magnesium alloy, Mater. Des. 59 (2014) 466–474.
[38] G.T. Zhao, Z.R. Zhang, Y.X. Zhang, H.L. Peng, Z. Yang, H. Nagaumi, X.Y. Yang, Effects of hot compression on the fracture toughness and tensile creep behaviors of a Mg-Gd-Y-Zn-Zr alloy, Mater. Sci. Eng. A 834 (2022) 142626.
[39] P. Guo, Y.Q. Zhao, W.D. Zeng, Q. Hong, The effect of microstructure on the mechanical properties of TC4-DT titanium alloys, Mater. Sci. Eng. A 563 (2013) 106–111.
[40] Y.P. Zheng, W.D. Zeng, D. Li, Q.Y. Zhao, X.B. Liang, J.W. Zhang, X. Ma, Fracture toughness of the bimodal size lamellar O phase microstructures in Ti-22Al-25Nb (at %) orthorhombic alloy, J. Alloys and Compd. 709 (2017) 511–518.
[41] A. Gutierrez, M. Hahn, Y.J. Li, A. Dehbozorgi, W. Hohorst, M. Schwartz, J. Orlita, Y.T. Hein, N. Guanzon, X.D. Sun, O.S. Es-Said, The effect of different annealing

conditions on the anisotropy of the fracture toughness of Ti-6Al-4V, J. Mater. Eng. Perform. 28 (2019) 7155–7164.
[42] D. Sampath, R. Akid, R. Morana, Estimation of crack initiation stress and local fracture toughness of Ni-alloys 945X (UNS N09946) and 718 (UNS N07718) under hydrogen environment via fracture surface topography analysis, Eng. Fract. Mech. 191 (2018) 324–343.
[43] R.Q. Cao, Q. Yu, J. Pan, Y. Lin, A. Sweet, Y. Li, R.O. Ritchie, On the exceptional damage-tolerance of gradient metallic materials, Mater. Today 32 (2020) 94–107.
[44] A. Chapuis, J.H. Driver, Temperature dependency of slip and twinning in plane strain compressed magnesium single crystals, Acta Mater. 59 (2011) 1986–1994.
[45] Z.Y. Wang, C. Cochrane, T. Skippon, Q.S. Dong, M.R. Daymond, Dislocation evolution at a crack-tip in a hexagonal close packed metal under plane-stress conditions, Acta Mater. 164 (2019) 25–38.
[46] Y. Chong, M. Poschmann, R.P. Zhang, S.T. Zhao, M.S. Hooshmand, E. Rothchild, D. L. Olmsted, J.W. Morris, D.C. Chrzan, M. Asta, A.M. Minor, Mechanistic basis of oxygen sensitivity in titanium, Sci. Adv. 6 (2020) eabc4060.
[47] M. Knezevic, M. Zecevic, I.J. Beyerlein, J.F. Bingert, R.J. McCabe, Strain rate and temperature effects on the selection of primary and secondary slip and twinning systems in HCP Zr, Acta Mater. 88 (2015) 55–73.
[48] V. Perovic, G.C. Weatherly, The β to α transformation in a Zr-2.5 wt % Nb alloy, Acta Metall. 37 (1989) 813–821.
[49] B.Y. Liu, N. Yang, J. Wang, M. Barnett, Y.C. Xin, D. Wu, R.L. Xin, B. Li, R. L. Narayan, J.F. Nie, J. Li, E. Ma, Z.W. Shan, Insight from in situ microscopy into which precipitate morphology can enable high strength in magnesium alloys, J. Mater. Sci. Technol. 34 (2018) 1061–1066.
[50] S.X. Huang, Q.Y. Zhao, Y.Q. Zhao, C. Lin, C. Wu, W.J. Jia, C.L. Mao, V. Ji, Toughening effects of Mo and Nb addition on impact toughness and crack resistance of titanium alloys, J. Mater. Sci. Technol. 79 (2021) 147–164.
[51] X.D. Zheng, S.J. Zheng, J. Wang, Y.J. Ma, H. Wang, Y.T. Zhou, X.D. Shao, B. Zhang, J.F. Lei, R. Yang, X.L. Ma, Twinning and sequential kinking in lamellar Ti-6Al-4V alloy, Acta Mater. 181 (2019) 479–490.
[52] J.W. Zhang, B. Leu, M.A. Kumar, I.J. Beyerlein, W.Z. Han, Twin hopping in nanolayered Zr-2.5Nb, Mater. Res. Lett. 8 (2020) 307–313.